Nanoscale

PAPER

View Article Online
View Journal

Published on 02 August 2017. Downloaded by University of Tennessee at Knoxville on 14/08/2017 21:56:08.

Check for updates

Cite this: DOI: 10.1039/c7nr04267a

Bromine substitution improves excited-state dynamics in mesoporous mixed halide perovskite films†

Eric M. Talbert,‡[a] Holly F. Zarick,‡[a] Abdelaziz Boulesbaa,[b] Naiya Soetan,[a] Alexander A. Puretzky,[b] David B. Geohegan[b] and Rizia Bardhan *[a]

Received 14th June 2017,
Accepted 29th July 2017

DOI: 10.1039/c7nr04267a

rsc.li/nanoscale

In this study, ultrafast transient absorption spectroscopy (TAS) is utilized to examine the excited-state dynamics in methylammonium lead iodide/bromide ($MAPb(I_{1-x}Br_x)_3$) perovskites as a function of bromide content. TAS spectral behavior reveals characteristic lifetimes for thermalization, recombination, and charge carrier injection of $MAPb(I_{1-x}Br_x)_3$ from x = 0 to 0.3 infiltrated in mesoporous titania films. Carrier recombination and charge injection lifetimes demonstrated a discernable increase with Br content likely because high carrier populations are supported by the higher density of vacant electronic states in mixed-halide perovskites due to the increased capacity of the conduction band. However, we observe for the first time that carrier thermalization lifetimes significantly decrease with increasing Br. This suggests that the shift in crystal structure from tetragonal towards pseudocubic accelerates carrier cooling, resulting in the relief of the hot phonon bottleneck. Furthermore, the stabilized $MAPb(I_{1-x}Br_x)_3$ samples exhibit a lower Burstein–Moss shift of 0.07–0.08 eV compared to pure $MAPbI_3$ (0.12 eV). Our results provide evidence that Br inclusion contributes to a broadening of the parabolic conduction band and to improvement in electron–phonon coupling and phonon propagation in the lattice.

Introduction

Photovoltaic devices designed with organic–inorganic halide perovskites have recently attained power conversion efficiencies (PCEs) reaching 22%,[1–3] demonstrating the promise of these low-cost materials for commercial viability and application in utility scale power. In this family of materials, methylammonium lead triiodide ($MAPbI_3$) perovskites have shown extraordinary performance due to their long range ambipolar diffusion lengths, large absorption coefficients, low exciton binding energies, and favorable band energetics.[4–6] However, the rapid degradation of $MAPbI_3$ in ambient air and moisture has resulted in poor long-term stability and undesirable hysteresis.[7,8] Several approaches have been adopted to surmount the stability issues, including device encapsulation with hydrophobic polymers and inorganic oxides[9,10] as well as engineering the charge transport layers to be water-resistant.[11,12] Alternatively, controllable substitution of $MAPbI_3$ perovskite with Br ions not only provides a straightforward and effective route to improve their moisture stability, but also enables tunable optical band gaps with minimal impact on the overall light absorption that can be controlled by Br ionic content.[13] The enhanced stability of mixed halide $MAPb(I_{1-x}Br_x)_3$ perovskites results from the smaller ionic radius of Br ions that shifts the lattice structure from tetragonal to pseudocubic and reduces the lattice parameter, restricting the diffusion of water into methylammonium vacancies.[14] The inclusion of Br ions has also shown to promote linear charge transport, giving rise to increased exciton diffusion lengths as well as reduced carrier recombination.[15–17] Relative to their pure iodide counterparts, the increased band gap of $MAPb(I_{1-x}Br_x)_3$ perovskites also results in higher open circuit voltages in the range of 1–1.5 V.[18,19] Therefore, by controllably infusing Br into the triiodide perovskite, moisture stability can be improved while preserving high photovoltaic performance.[20]

Recent work on mixed halide perovskites has focused on their synthesis and measurements of crystallization kinetics,[21,22] band gap engineering of their optical properties,[23]

[a]Department of Chemical and Biomolecular Engineering, Vanderbilt University, Nashville, TN 37235, USA. E-mail: rizia.bardhan@vanderbilt.edu
[b]Center for Nanophase Materials Sciences, Oak Ridge National Laboratory, Oak Ridge, TN 37831, USA

†Electronic supplementary information (ESI) available: Top view SEM images, glancing angle XRD measurements, and estimated grain size as a function of Br content calculated with the Scherrer equation. Also provided are power dependent measurements, including full TAS spectra for each sample at four different excitation energies, and tables of amplitudes and lifetimes calculated from exponential fits of TAS data. See DOI: 10.1039/c7nr04267a

‡Equal contributing first authors.

Published on 02 August 2017. Downloaded by University of Tennessee at Knoxville on 14/08/2017 21:56:08.

increasing their environmental stability,[20,24,25] and correlating their structural and luminescent properties.[26–28] Despite this extensive work, the impact of halide composition on carrier thermalization and transport is not fully understood. While time-resolved photoluminescence (tr-PL) spectroscopy has been employed to study these fundamental parameters, tr-PL characterizes emissive states and cannot probe dark (non-emissive) states, which play a critical role in the light absorption properties of perovskites. Further, tr-PL also cannot resolve sub-picosecond carrier processes occurring in perovskites due to detection speed limitations. On the other hand, ultrafast pump–probe transient absorption spectroscopy (TAS) can reveal high resolution spectral and temporal behavior of photogenerated species and resolve the time scales of various excited state processes, and has been utilized to study perovskites extensively.[29–32] Whereas time-resolved studies of carrier relaxation dynamics in pristine perovskite films (or those paired with a non-interacting scaffold) have already been reported,[32–35] this study particularly probes mixed halide perovskites infiltrated in mesoporous TiO_2 films. We employed TAS to understand the impact of halide composition on the timescales of carrier thermalization, carrier recombination, and charge injection at the perovskite/TiO_2 interface in MAPb$(I_{1-x}Br_x)_3$ perovskite/TiO_2 films. Our motivation to study perovskite/TiO_2 films stems from examining the literature where some of the most promising high efficiency devices are achieved with perovskites infiltrated in mesoporous TiO_2 scaffolds.[36–38] Therefore, probing the fundamental mechanisms in this system is highly relevant to understanding the driving forces in high performing solar devices. Our TAS results from mesoporous mixed halide perovskites show that carrier cooling and relaxation dynamics within a mesoporous TiO_2 architecture are favorably affected by bromide inclusion. We demonstrate for the first time that the TAS bleach formation kinetics, attributed to hot carrier thermalization, are accelerated with increasing Br content, indicating relief of the hot phonon bottleneck. Conversely, the bleach relaxation, modeled by two characteristic lifetimes representing Auger recombination and charge injection to TiO_2, slows with increasing Br composition. Finally, the Burstein–Moss shift, which describes energetics within the conduction band and is evaluated from the position of the bleach feature, decreases with the addition of Br as the capacity of the conduction band increases. Our work provides a mechanistic understanding of the carrier accumulation and carrier decay processes in mixed halide perovskites within a mesoporous TiO_2 architecture.

Experimental methods

All reagents, unless otherwise specified, were purchased from Sigma Aldrich and used as received without further purification. All H_2O used for substrate preparation was ultrapure H_2O (18.2 MΩ) obtained from a Milli-Q Direct-Q 3UV system. All work done under inert atmosphere was conducted in an MBraun LabStar glovebox filled with nitrogen (<0.5 ppm O_2).

Precursor synthesis

Methylammonium bromide (MABr) and methylammonium iodide (MAI) were synthesized according to previously reported procedures.[39,40] Separately, 32.3 mL of hydroiodic acid (37 wt% in H_2O) was combined with 30 mL of methylamine (40% in methanol, TCI) and 44 mL of hydrobromic acid was combined with 27.8 mL of methylamine to produce MAI and MABr, respectively. Both were reacted at 0 °C for two hours under stirring using an ice bath. After two hours, the solutions were evaporated at 55 °C using a rotovap. The precipitates were each washed at least 3× with diethyl ether and then collected using vacuum filtration. Finally, the crystals were dried in a vacuum oven at 60 °C for 24 hours before use.

Perovskite layer fabrication

Thin mesoporous TiO_2 layers infiltrated with MAPb$(I_{1-x}Br_x)_3$ were fabricated on either 1″ squares of Pilkington TEC 15 FTO glass for imaging characterizations or microscope glass for optoelectronic and XRD characterizations. Glass and FTO-glass substrates were cleaned by sonication for 30 minutes in a 2 vol% solution of Hellmanex in H_2O, rinsed with H_2O and IPA, sonicated for an additional 15 minutes in a 1 : 1 v/v mixture of IPA/acetone, rinsed with IPA, dried with N_2, and finally plasma treated for 15 minutes immediately before use. A ~50 nm layer of compact TiO_2 was deposited on the substrates by hydrolyzing 40 mM $TiCl_4$ at 70 °C for 60 minutes. After substrates were removed from the $TiCl_4$ bath, they were rinsed with H_2O and EtOH, dried with N_2, and then annealed at 100 °C for 10 minutes and 500 °C for 15 minutes. A ~100 nm mesoporous TiO_2 layer was deposited by spin coating 250 μL of a diluted 18NRT Dyesol paste solution (3 : 6 : 1 by weight of EtOH : α-terpineol : Dyesol) at 500 RPM for 5 s and 6000 RPM for 40 s, dried on a 100 °C hot plate, and then sintered at 500 °C for 30 minutes. Once cooled, the mesoporous layers received a 40 mM $TiCl_4$ post-treatment for 30 minutes at 70 °C, were rinsed with H_2O and EtOH, dried with N_2, and fired in air at 500 °C for 15 minutes. MAPb$(I_{1-x}Br_x)_3$ was deposited on the mesoporous scaffold by modifying a two-step sequential deposition process previously described.[41] Substrates were transferred into an inert atmosphere environment. A 100 mg mL^{-1} solution of PbI_2 in *N*,*N*-dimethylformamide was stirred vigorously for 1 hour at 70 °C to dissolve before use. 200 μL was deposited onto each substrate and left to sit for ~5 s to ensure that the solution was infiltrated throughout the full thickness of the mesoporous TiO_2 before spin coating at 500 RPM for 5 s and 6000 RPM for 40 s, followed by a 30 minute annealing at 70 °C. Once cooled post-annealing, substrates were dipped in IPA for 1–2 s before being placed in a bath containing the appropriate stoichiometric ratios of MAI and MABr in IPA, each on the range of ~15 mg mL^{-1} (see Table S1† for full details), for 1 minute with swirling, rinsed thoroughly with IPA, and annealed again at 75 °C for 30 minutes.

Materials characterization

All optical absorbance spectra were taken using a Varian Cary 5000 UV-vis NIR spectrophotometer. Band gaps were estimated

 This journal is © The Royal Society of Chemistry 2017

Published on 02 August 2017. Downloaded by University of Tennessee at Knoxville on 14/08/2017 21:56:08.

using Tauc plots, extrapolating the tangent to the steepest point of the absorbance band edge to where it crosses the baseline absorbance level and using the following relation: $E_g = hc/\lambda_{Tauc}$. Scanning electron micrographs were taken with a Zeiss Merlin at 10 kV accelerating voltage. Glancing angle X-ray diffraction spectra were obtained with a Scintag XGEN4000 X-ray diffractometer with CuK_α at wavelength λ = 0.154 nm, and analysis is focused on the 2θ = 15° peak because of its indication of offset from cubic crystallinity. Grain size was estimated using the Scherrer equation with K = 1:

$$d = \frac{K\lambda}{\mathrm{FWHM} \times \cos\theta} \quad (1)$$

Transient absorption measurements

Femtosecond transient absorption measurements were conducted using a home-built pump–probe setup based on a femtosecond laser system, that utilizes seed pulses from a titanium sapphire oscillator (Micra, Coherent), amplified by a Ti: Sapphire amplifier (Legend USP-HE, Coherent) to provide 800 nm femtosecond pulses (2.5 mJ per pulse), operating at 1 kHz repetition rate with ~45 fs pulse durations. The Legend amplifier is pumped by a Nd:YLF laser (Evolution-30, Coherent). A small portion of the output of the amplifier (~4 μJ per pulse) is focused on a sapphire window (2 mm thick) to generate a white light continuum (WLC) probe (450–900 nm). To minimize temporal chirp in the spectrally broad WLC probe, a set of parabolic mirrors was used to collimate and focus the WLC on the sample. The transmitted probe was focused onto 100 μm core fiber coupled with a spectrometer/CCD (USB2000ES, Ocean Optics). The pump pulse at 400 nm is generated by doubling ~50 μJ per pulse of the 800 nm fundamental in a BBO crystal. The pump beam passes through a delay line to allow control of time delay between the pump and the probe. In order to measure absorbance changes between every two successive laser shots, the pump beam was chopped at a frequency of 500 Hz. At the sample, the spot sizes of the pump and probe pulses were 100 μm and 50 μm, respectively. The pulse energy of the pump was varied between 20, 40, 60, and 80 μJ per pulse using a variable neutral density filter, corresponding to energy fluences at the sample of ~28.4, 56.8, 85.2, and 113.6 μJ cm^{-2}. Amplitudes and lifetimes were extracted by fitting the integrated PB1 peak intensity to a convolution of the excitation Gaussian pulse to the following multiexponential function which contains a positive exponential component for extracting bleach formation, and two negative components to describe the bleach recovery:

$$\Delta\mathrm{OD} = A_0 e^{-t/\tau_0} - A_1 e^{-t/\tau_1} - A_2 e^{-t/\tau_2} \quad (2)$$

To account for temporal chirp, the absolute times of measurement data were adjusted by wavelength based on the earliest observed response time. Peaks were integrated from the time-adjusted data set, and the normalized peak areas were fit over time to obtain kinetic parameters. The centroid of the peak areas was tracked as the Fermi energy of conduction band electrons. Residuals were calculated to check for goodness of fit; corresponding R-squared values can be found in Table S2.† All R-squared values are in the range of ~0.98 and above, which shows good reliability.

Results and discussion

The $MAPb(I_{1-x}Br_x)_3$ perovskite films were synthesized by varying the I/Br ratios in a mixed halide precursor solution (Table S1†) and infiltrating the perovskites in a 100 nm mesoporous TiO_2 (mp-TiO_2) layer with an additional 100 nm perovskite overlayer. The mp-TiO_2 layer provides a scaffold for formation of the perovskite crystals, allows a precise way to control perovskite thickness, and provides an electron acceptor for carrier injection from the perovskites following optical excitation. The I/Br ratio was controlled by the relative concentrations of the MAI/MABr soak solution for PbI_2-infiltrated mp-TiO_2 substrates, as detailed in the Experimental methods and Table S1,† and the exact Br content was further confirmed *via* XRD and UV-vis absorption measurements. Investigation of Br substitution was capped at x = 0.3, as previous studies have found that any improvements in optoelectronic properties of $MAPb(I_{x-1}Br_x)_3$ are negated past 30% Br inclusion as light absorption decreases sharply.[42,43] Additionally, in our experiments, we found that with Br compositions higher than x = 0.3, the average grain size increased at the expense of complete coverage and contact with the mp-TiO_2 scaffold. While the thickness of both layers is significantly lower than that used in typical perovskite solar cells,[44,45] these thicknesses were chosen to achieve relatively consistent optical density (OD ~ 1.0–1.25 at 400 nm) between samples, providing ample transmittance for TAS measurements even at near-complete perovskite coverage. A representative top view and cross-sectional view of $MAPbI_3$ perovskite film are shown in Fig. 1a and b, respectively. Top-view SEMs of all other Br content samples are shown in Fig. S1,† verifying that grain structure and coverage are sufficiently similar across all Br compositions. A non-color modified version of Fig. 1b can be found in Fig. S2 in the ESI.†

While the grain structure in the different $MAPb(I_{1-x}Br_x)_3$ samples is similar across all Br compositions, the lattice microstructure differs due to the size difference between I and Br ions. As I ions are displaced by smaller Br ions, the lattice parameter decreases as the lattice shifts from a tetragonal structure toward a pseudocubic geometry, evidenced by the (110) peak shift toward 2θ = 15° with increasing Br in normalized XRD spectra (Fig. 1c). The peak shifts align with those observed in literature for $MAPb(I_{1-x}Br_x)_3$,[28,46] confirming the presence of $MAPb(I_{1-x}Br_x)_3$ at the desired Br compositions. The absence of impurity peaks in full XRD spectra (Fig. S3†) further confirms the purity of the perovskite phase and minimal unreacted PbX_2 present in any sample. Moreover, the average crystallite diameter, calculated from the (110) peak width using the Scherrer equation, is relatively constant for all Br compositions (Fig. S4†). The pure $MAPbI_3$ (0% Br) sample shows slightly elevated microstructure size compared to

Published on 02 August 2017. Downloaded by University of Tennessee at Knoxville on 14/08/2017 21:56:08.

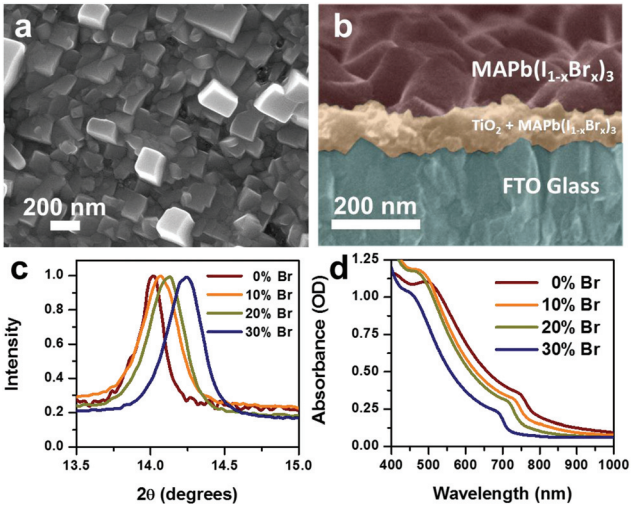

Fig. 1 Representative top-view SEM (a) and cross-sectional SEM (b) of a 100 nm mp-TiO_2 layer infiltrated with $MAPb(I_{1-x}Br_x)_3$. Shown here is x = 0 Br incorporation for both (a) and (b). (c) Glancing angle XRD peaks normalized to the (110) plane for $MAPb(I_{1-x}Br_x)_3$ mesoporous film samples with increasing Br content. (d) Optical absorbance spectra of all four samples.

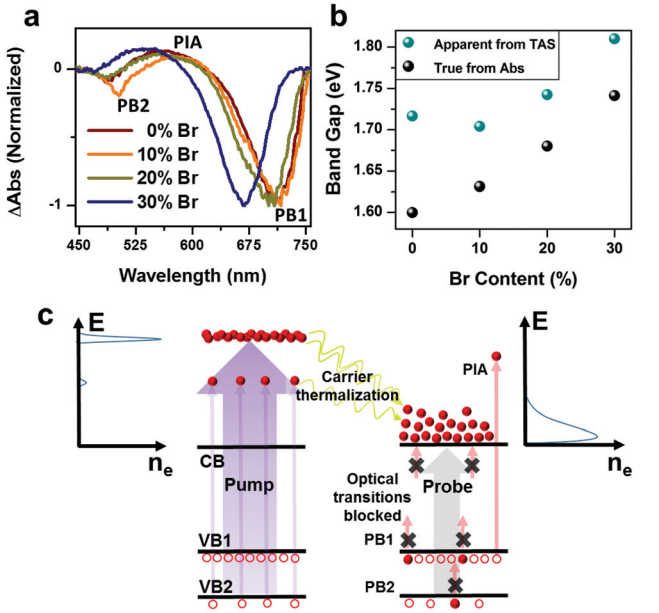

Fig. 2 (a) Transient absorption spectra for all samples showing two distinct photobleaches near 700 nm and 500 nm corresponding to PB1 and PB2, respectively, and a broadband photoinduced absorption (PIA) in between. Spectra are normalized at the maximum peak of PB1 (~3 ps time delay). (b) Bandgaps calculated from absorbance band edges and transient absorption evolution of PB1, separated by the Burstein–Moss shift. (c) Energy diagram of excited-state processes initiated in TAS, where n_e is the number of conduction band electrons and E is energy above the bandgap. A 400 nm laser pumps electrons (solid circles) into the conduction band (CB), leaving holes (hollow circles) in the valence bands (VB). Carriers thermalize to a quasi-equilibrium distribution, where the optical transitions of a white-light probe are either bleached (PB) or enhanced (PIA) depending on photon energy.

bromide-containing perovskite films, indicating that there is some compositional heterogeneity within mixed halide perovskite grains. However, based on the steepness of the absorbance band edge (Fig. 1d), we conclude that this compositional heterogeneity arises from a natural dispersion of I and Br ions during the two-step perovskite synthesis. In addition to the crystallographic and topographic characterization of the perovskites, we have also probed the optical properties of the mixed halide perovskite films. Prior to analysis of transient absorption spectra, it is essential to understand the optical behavior of perovskites, as the excited-state deviations revealed by TAS highlight excitonic features present in the absorbance spectra of the $MAPb(I_{1-x}Br_x)_3$ films. The absorbance spectra shown in Fig. 1d demonstrate similar optical density for all Br compositions and a predictable blue shift of the absorptive band edge with increasing Br content.[47,48]

TAS measurements were recorded at a time delay after an excitation pulse saturates the perovskite conduction band, and show the absolute deviation in absorbance from the ground-state absorbance spectra. The TAS spectra for all samples at a time delay of 3 ps after excitation is shown in Fig. 2a when photobleach (PB) and photoinduced absorption (PIA) features are near their maximum. The broad PIA between 500–600 nm represents increased photoexcitation at off-peak wavelengths due to conduction band saturation.[49,50] The PIA has also recently been linked to refractive index changes induced by the free carrier population, as photoexcited states in all semiconductors result in variations in the dielectric function.[50] There are two distinct photobleaches, PB1 at ~700 nm and PB2 at ~500 nm, which have been described by a dual valence and common conduction band model for $MAPbI_3$. This two valence band model was first proposed by Xing *et al.* as a possible route for the formation of the two photobleach states.[51] These photobleaches represent blocked optical transitions from the two valence bands excited to the conduction band by the pump pulse.[49,50,52,53] The optical transitions behind these features are depicted schematically in Fig. 2c, where the PB1 band reflects the transition from VB1 to CB, and PB2 reflects the transition from VB2 to CB. The intensity of PB2 has been attributed to both the presence of PbI_2 impurity and to charge injection into TiO_2.[50,52] Because the PB2 is primarily dependent on impurity presence rather than on bulk phase charge transport, our work focuses on the dynamics of the PB1 photobleach.

Following the ultrafast excitation of perovskites, carrier thermalization results in accumulation of the carrier population at energy levels near the band gap (Fig. 2c). Carriers naturally thermalize to the minimum band energy, which is bound by a characteristic parabolic band shape, before recombining. However, since the density of states in the conduction band is finite, thermalized carriers adopt a Fermi–Dirac distribution above the parabolic boundary. After the 400 nm pump pulse creates a nonequilibrium distribution of excited electrons in the conduction band, electron–phonon coupling cools the carriers to a stable energy distribution within a couple of

 This journal is © The Royal Society of Chemistry 2017

Published on 02 August 2017. Downloaded by University of Tennessee at Knoxville on 14/08/2017 21:56:08.

picoseconds. This distribution follows the parabolic band shape that is centered slightly above the absorption band edge due to the Burstein–Moss effect. The Burstein–Moss model of electronic band filling takes into account the broadening of the PB1 band, which is indicative of charge carrier accumulation and correlates the change in optical band gap to the charge density raised to the power of 2/3.[49,54] Since excitation into the conduction band is blocked by the equilibrium distribution of filled electronic states, a photobleach is observed in the white-light continuum probe corresponding to the band gap energies with reference to the valence band. The apparent band gap for the blocked optical transitions in TAS is calculated from the centroid of the integrated TAS spectra[49,50] and compared to the band gap from absorption in Fig. 2b. The difference between the band gaps as evaluated from TAS and absorption measurements represents the Burstein–Moss shift. The mixed halide samples (10–30% Br) show a consistent Burstein–Moss shift around 0.07–0.08 eV, but the pure iodide sample has a much higher Burstein–Moss shift of 0.12 eV. Based on the evolutionary spectra of all samples (Fig. S5–S8†) we do not anticipate that a significant portion of the bleach feature is cut off by the low-pass filter; therefore, the bleach centroid position adequately represents the mean energy of the carrier population for all samples. More importantly, the measured conductivity of pure $MAPbI_3$ perovskite has been reported to be lower than that of bromide-containing perovskites,[26,55] which suggests that parabolic conduction bands of $MAPbI_3$ have lower density of vacant electronic states available for free carriers. Thus, the energy distribution of fully pumped $MAPbI_3$ samples is shifted higher above the band gap. This is further explained below in the discussion of bleach formation lifetimes, which are markedly longer for the thermalization of carriers in $MAPbI_3$ than in $MAPb(I_{1-x}Br_x)_3$.

Carrier cooling can be tracked by the PB1 formation in TAS, which occurs within the first 2 ps after photoexcitation as shown in Fig. 3a. The lifetimes for bleach formation, τ_0, are obtained from an exponential fit with positive amplitude, and a standard pulse width of 0.1 ps is fixed to account for the laser attenuation at early times. To understand the impact of the pump power on the thermalization lifetimes of the Br substituted mixed-halide perovskite samples, power dependent measurements were conducted between 20 and 80 μJ per pulse. The thermalization lifetime increases (*i.e.* the carrier cooling rate decreases) with rising pump fluence for all $MAPb(I_{1-x}Br_x)_3$ samples, as shown in Fig. 3b. With increasing pump fluence, the number of absorbed photons increases as well, resulting in high occupancy of energy levels nearest the band edge. The abundance of hot carriers, as well as the limit of phonon–electron coupling, inhibits the relaxation of carriers from the initial excited state to the conduction band edge, resulting in an enhanced hot carrier population.[56] This impediment to the carrier cooling in perovskites is a phenomenon described as the hot phonon bottleneck effect.[57–59] The clear trends observed in carrier thermalization with pump power indicate that hot phonon bottleneck is observable in the pure iodide and mixed halide perovskite mesoporous films.

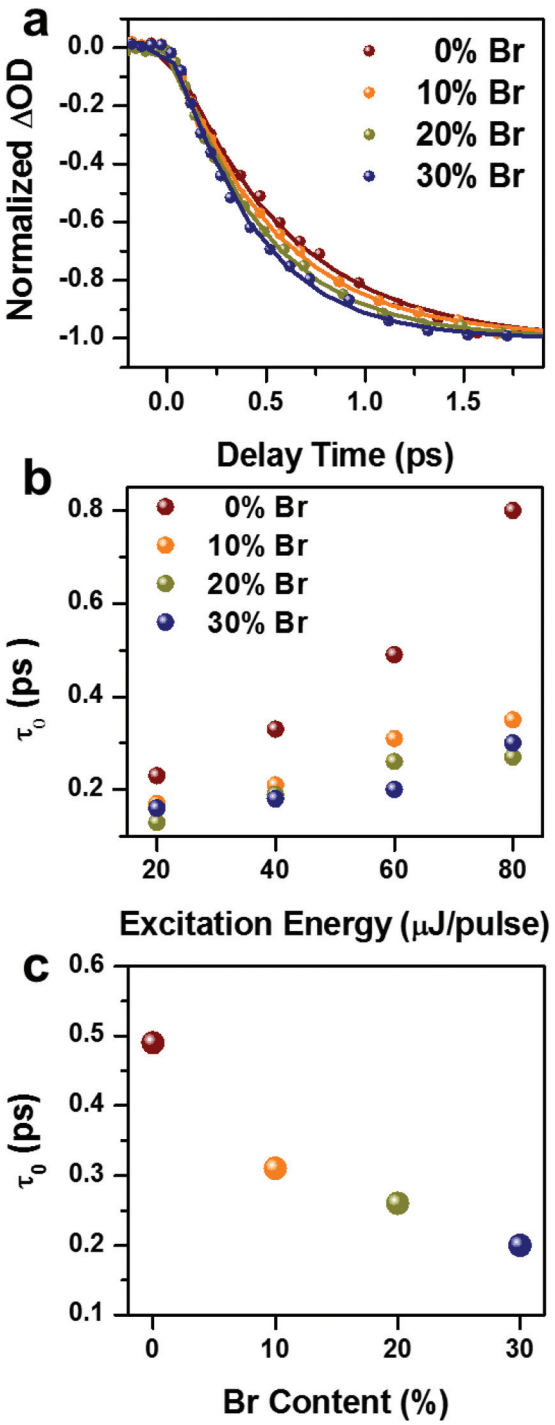

Fig. 3 (a) Early time scales of TAS dynamics showing bleach formation dynamics of PB1 as a function of Br content. Experimental data (symbols) shown with an exponential fit (smooth lines) as described in the experimental methods. Thermalization lifetimes, τ_0, extracted from exponential fits of the samples are given as a function of excitation fluence in (b) and a function of Br content (c). The excitation fluence for the data shown in (a) and (c) was 60 μJ per pulse.

Whereas phonon bottleneck is strongest in the $MAPbI_3$ sample indicating a long-lived population of hot carriers, with increasing Br substitution in the perovskite lattice the phonon bottle-

Published on 02 August 2017. Downloaded by University of Tennessee at Knoxville on 14/08/2017 21:56:08.

neck effect slightly diminishes. This observation is clearly indicated in Fig. 3c (also shown in Fig. S9† for all excitation fluences) showing that carrier thermalization rates become more rapid with increasing bromide composition. Our results therefore suggest that the hot phonon bottleneck is being relieved with bromine substitution, reducing the number of hot carriers with increasing Br content. Cooling of hot carriers in semiconductors dissipates the excess absorbed optical energy as lattice heat, comprising 50% of energy losses in traditional solar devices.[60] Therefore, the faster carrier thermalization in Br-substituted perovskites likely assists with device cooling and improve device longevity. However, in high power optoelectronics such as lasing and photodetection where a high population of hot carriers is useful, the pure iodide perovskite will be more desirable. The trends in Fig. 3c also illustrate that the most substantial decrease in τ_0 occurs between 0% and 10% Br, which further suggests that even low concentrations of Br improve electron–phonon coupling within the mixed lattice of $MAPb(I_{1-x}Br_x)_3$. The mechanism of this stability arises from the local crystalline geometry around Br ions. Since the $MAPbBr_3$ perovskite adopts a nearly perfect cubic lattice,[61,62] the Pb centers in the PbX_6 octahedra will align linearly across the Br ions. This localized alignment is expected to promote phonon propagation as well as electron–phonon coupling.[63] As the Br concentration is further increased, the electron–phonon coupling improves incrementally as more PbX_6 octahedra are linearly aligned. Beyond improved charge transport,[27,64] the presence of Br ions in $MAPb(I_{1-x}Br_x)_3$ perovskites modifies the conduction band structure to enable faster carrier thermalization and phonon diffusion.[65,66]

The PB1 decay was also studied by fitting integrated peaks to two distinct decay exponents, a fast (τ_1) and slow (τ_2) component, from a biexponential fit (Fig. 4a). Here, τ_1 is attributed to both charge carrier trapping at perovskite grain boundaries or defect sites and Auger recombination. The relatively high pump fluence (60 μJ per pulse) indicates that the carrier density is high enough that Auger recombination likely dominates τ_1. This correlates well to previous findings by Xing *et al.*[51] suggesting the high absorption coefficient and long carrier diffusion lengths in organolead perovskites necessitates the use of low pump fluence to minimize energy losses by Auger recombination. Table S2 in the ESI† illustrates both a decrease in τ_1 as well as an increase in amplitude (A_1) with increasing pump fluence, indicating increased dominance of Auger recombination over trap-assisted recombination at high laser power.[50,67,68] The time constants for carrier recombination show a small increase for Br > 10% (Fig. 4b). While in thin films of pure MA-Pb halides without a mesoporous scaffold, an increase in Auger recombination rate has been observed in $MAPbBr_3$ perovskites attributed to their higher exciton binding energy relative to $MAPbI_3$,[69] we observe only a weak increase in the Auger-dominated τ_1 with increasing Br content in $MAPb(I_{1-x}Br_x)_3/mp\text{-}TiO_2$ films within the x = 0 to 0.3 studied here. This observation is expected because high carrier populations are supported by the higher density of vacant electronic states in Br-containing perovskites due to the increased capacity of the conduction band.[26,55] The slow decay component, τ_2, represents charge injection from the perovskite to the mesoporous TiO_2 substrate that occurs on a time scale of hundreds of picoseconds.[31,70] We observe a gradual increase in the charge injection time constant with increasing Br content (Fig. 4c), which is expected due to the marginally close energy alignment between the conduction band of TiO_2 and the pure triiodide perovskite (~0.1 eV). Park *et al.* have shown that for Br compositions up to 30% the conduction band edge increases by ~0.05 eV; this small increase is likely responsible for delaying charge injection as bromide composition increases.[27] We note that while time-resolved photoluminescence can probe mechanisms that occur at nanosecond timescales, such as recombination within isolated bulk perovskites,[18,20,70] the sub-picosecond resolution of TAS is ideal for studying rapid processes, including thermalization and carrier trapping within mesoporous films.

The progression of the carrier recombination processes also impacts the energy distribution of the excited-state carriers,[71] as schematically depicted in Fig. 5a. Auger and trap-assisted

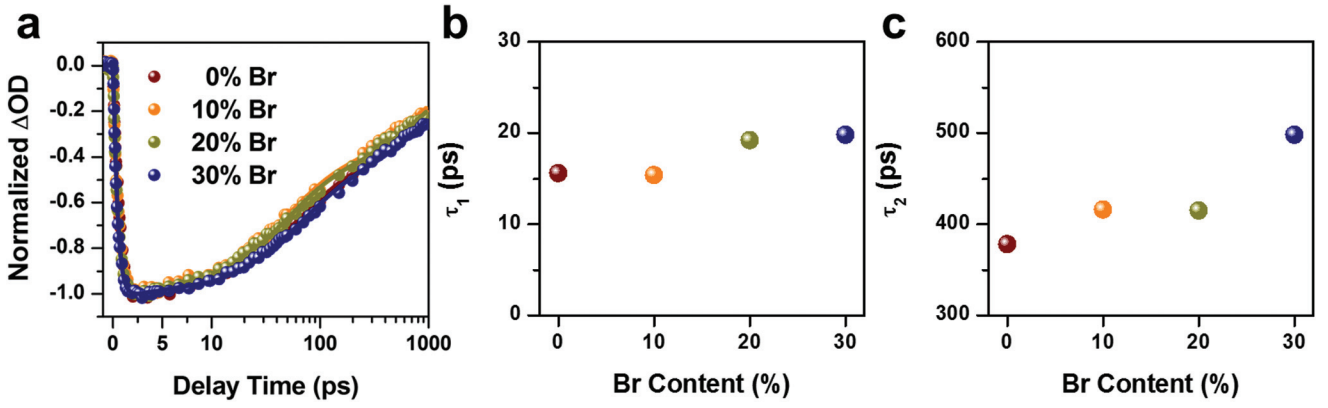

Fig. 4 (a) Full dynamics of integrated PB1 intensity (symbols) fit with a biexponential decay function (solid line). (b) Auger recombination lifetimes, τ_1, measured at the pump fluence of 60 μJ per pulse and (c) charge injection lifetimes, τ_2, extracted from the exponential fits suggest that bromide content has a limited effect on recombination mechanisms in thin mesoporous films.

 This journal is © The Royal Society of Chemistry 2017

Published on 02 August 2017. Downloaded by University of Tennessee at Knoxville on 14/08/2017 21:56:08.

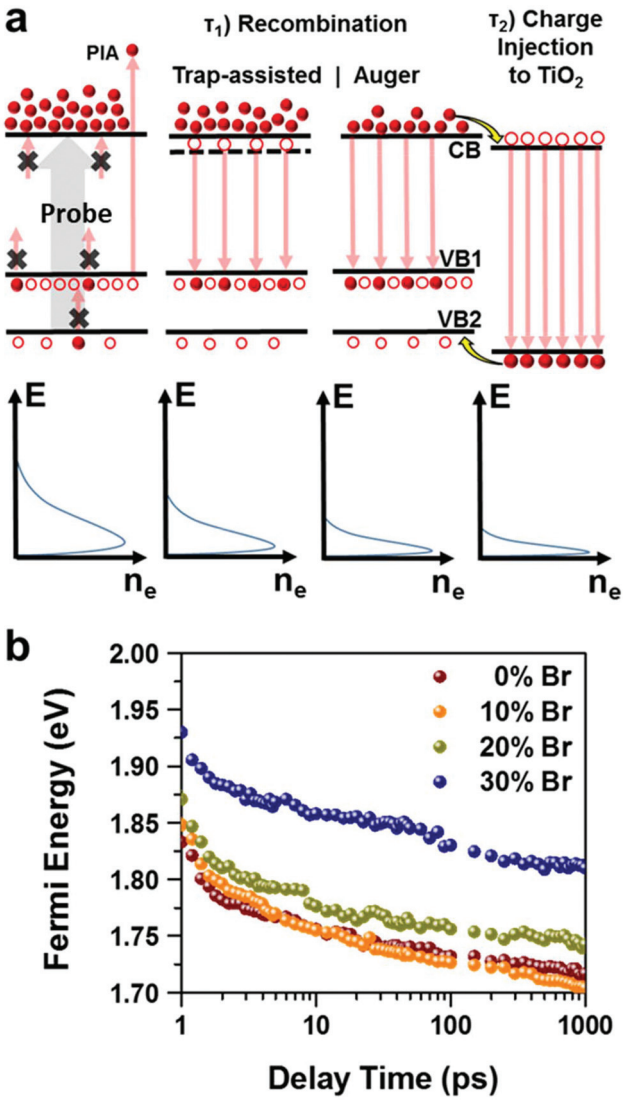

Fig. 5 (a) Energy diagram illustrating decay processes for photogenerated carriers. Photoexcitation of perovskites pumps electrons from valence bands (VB) into the conduction band (CB). Carriers decay by either injecting into TiO_2 or relaxing *via* trap-assisted (one-body) or Auger (multi-body) recombination mechanisms. (b) The Fermi energy of excited carriers, calculated from the centroid of integrated PB1 features, decreases as the carrier population relaxes over time.

recombination, correlating to time constant τ_1, contribute to about half of the observed excited-state decay. The majority of the remaining amplitude decays by the slower time constant, τ_2, representing carrier injection from the perovskite to TiO_2. The Fermi energy of excited carriers, calculated from the integrated PB1 peak position, is tracked over time in Fig. 5b to show the regression of mean carrier energy toward the Burstein–Moss limit. The sharp decline in Fermi energy at early timescales is a remnant of carrier thermalization, stabilizing around 3 ps when conduction electrons have relaxed to thermal equilibrium. The Fermi energy then continues to decline gradually as the carrier population is depleted. The slope of the decrease in Fermi energy shows very small variations between samples since τ_1 shows a weak variation across bromide compositions. However, the Fermi energy of pure $MAPbI_3$ approaches an apparent minimum consistent with the hypothesis that narrow-banded $MAPbI_3$ perovskites exhibit a greater Burstein–Moss shift than the mixed halide MAPb $(I_{1-x}Br_x)_3$ samples.

Conclusions

In summary, we utilized TAS to probe the excited-state dynamics of $MAPb(I_{1-x}Br_x)_3$ mixed halide perovskites in a thin mp-TiO_2 film geometry. The TAS dynamics were well fit by a multi-exponential fit representing lifetimes for sub-picosecond thermalization, picosecond carrier trapping and recombination, and sub-nanosecond charge injection to TiO_2, respectively. The measurements reveal that both Auger-dominated carrier recombination and charge injection lifetimes show weak increase with rising bromide compositions between 0–30%. However, carrier thermalization rapidly improves by substituting Br in $MAPbI_3$, which we conclude enhances the electron–phonon coupling in the perovskite lattice. The observed faster carrier thermalization in Br-containing perovskite samples is attributable to relief of the hot phonon bottleneck and to the broadening of the parabolic conduction band with Br inclusion. This indicates that as low as 10% Br substitution in $MAPbI_3$ perovskites not only increases the stability of conduction band to energetic perturbations but also promotes efficient heat dissipation from the active layer with minimal impact on light absorption.[65] The fundamental insight gained from this work will not only enhance the understanding of the ultrafast carrier processes in organic–inorganic perovskites, but can also be applied to more complex systems such as such as interfaces of perovskites with other semiconductors or metal nanostructures.[72,73]

Acknowledgements

EMT acknowledges the VINSE fellowship and Vanderbilt start-up funds. HFZ acknowledges support from Vanderbilt University Discovery grant, and the Department of Education for Graduate Assistance in Areas of National Need (GAANN) Fellowship under grant number P0200A090323. TEM images were obtained with an instrument supported by NSF EPS 1004083. Ultrafast transient absorption measurements were conducted at the Center for Nanophase Materials Sciences, which is a DOE Office of Science User Facility.

References

1 N.-G. Park, M. Grätzel, T. Miyasaka, K. Zhu and K. Emery, *Nat. Energy*, 2016, **1**, 16152.
2 L. Atourki, E. Vega, B. Marí, M. Mollar, H. Ait Ahsaine, K. Bouabid and A. Ihlal, *Appl. Surf. Sci.*, 2016, **371**, 112–117.

Published on 02 August 2017. Downloaded by University of Tennessee at Knoxville on 14/08/2017 21:56:08.

3 M. A. Green, K. Emery, Y. Hishikawa, W. Warta and E. D. Dunlop, *Prog. Photovoltaics*, 2016, **24**, 905–913.
4 L. M. Pazos-Outón, M. Szumilo, R. Lamboll, J. M. Richter, M. Crespo-Quesada, M. Abdi-Jalebi, H. J. Beeson, M. Vrućinić, M. Alsari, H. J. Snaith, B. Ehrler, R. H. Friend and F. Deschler, *Science*, 2016, **351**, 1430–1433.
5 T. Leijtens, G. E. Eperon, A. J. Barker, G. Grancini, W. Zhang, J. M. Ball, A. R. S. Kandada, H. J. Snaith and A. Petrozza, *Energy Environ. Sci.*, 2016, **9**, 3472–3481.
6 S. Kazim, M. K. Nazeeruddin, M. Gratzel and S. Ahmad, *Angew. Chem., Int. Ed.*, 2014, **53**, 2812–2824.
7 D. Bryant, N. Aristidou, S. Pont, I. Sanchez-Molina, T. Chotchunangatchaval, S. Wheeler, J. R. Durrantab and S. A. Haque, *Energy Environ. Sci.*, 2016, **9**, 1655–1660.
8 Y. Rong, L. Liu, A. Mei, X. Li and H. Han, *Adv. Energy Mater.*, 2015, **5**, 1501066.
9 J. You, L. Meng, T.-B. Song, T.-F. Guo, Y. M. Yang, W.-H. Chang, Z. Hong, H. Chen, H. Zhou, Q. Chen, Y. Liu, N. D. Marco and Y. Yang, *Nat. Nanotechnol.*, 2015, **11**, 75–81.
10 I. Hwang, I. Jeong, J. Lee, M. J. Ko and K. Yong, *ACS Appl. Mater. Interfaces*, 2015, **7**, 17330–17336.
11 S. N. Habisreutinger, T. Leijtens, G. E. Eperon, S. D. Stranks, R. J. Nicholas and H. J. Snaith, *Nano Lett.*, 2014, **14**, 5561–5568.
12 J. H. Kim, P. W. Liang, S. T. Williams, N. Cho, C. C. Chueh, M. S. Glaz, D. S. Ginger and A. K. Jen, *Adv. Mater.*, 2015, **27**, 695–701.
13 S. A. Kulkarni, T. Baikie, P. P. Boix, N. Yantara, N. Mathews and S. Mhaisalkar, *J. Mater. Chem. A*, 2014, **2**, 9221–9225.
14 T. G. Kim, S. W. Seo, H. Kwon, J. Hahn and J. W. Kim, *Phys. Chem. Chem. Phys.*, 2015, **17**, 24342–24348.
15 J. Liu and O. V. Prezhdo, *J. Phys. Chem. Lett.*, 2015, **6**, 4463–4469.
16 B. Suarez, V. Gonzalez-Pedro, T. S. Ripolles, R. S. Sanchez, L. Otero and I. Mora-Sero, *J. Phys. Chem. Lett.*, 2014, **5**, 1628–1635.
17 J. H. Heo and S. H. Im, *Nanoscale*, 2016, **8**, 2554–2560.
18 Y. Zhou, F. Wang, H.-H. Fang, M. A. Loi, F.-Y. Xie, N. Zhao and C.-P. Wong, *J. Mater. Chem. A*, 2016, **4**, 16191–16197.
19 Y.-C. Hsiao, T. Wu, M. Li, Q. Liu, W. Qin and B. Hu, *J. Mater. Chem. A*, 2015, **3**, 15372–15385.
20 W. Zhu, C. Bao, F. Li, T. Yu, H. Gao, Y. Yi, J. Yang, G. Fu, X. Zhou and Z. Zou, *Nano Energy*, 2016, **19**, 17–26.
21 D. Bae, A. Palmstrom, K. Roelofs, B. Mei, I. Chorkendorff, S. F. Bent and P. C. Vesborg, *ACS Appl. Mater. Interfaces*, 2016, **8**, 14301–14306.
22 B. Yang, J. Keum, O. S. Ovchinnikova, A. Belianinov, S. Chen, M. H. Du, I. N. Ivanov, C. M. Rouleau, D. B. Geohegan and K. Xiao, *J. Am. Chem. Soc.*, 2016, **138**, 5028–5035.
23 D. M. Jang, K. Park, D. H. Kim, J. Park, F. Shojaei, H. S. Kang, J. P. Ahn, J. W. Lee and J. K. Song, *Nano Lett.*, 2015, **15**, 5191–5199.
24 Z. Wang, D. P. McMeekin, N. Sakai, S. van Reenen, K. Wojciechowski, J. B. Patel, M. B. Johnston and H. J. Snaith, *Adv. Mater.*, 2017, **29**, 1604186.
25 S. Dastidar, D. A. Egger, L. Z. Tan, S. B. Cromer, A. D. Dillon, S. Liu, L. Kronik, A. M. Rappe and A. T. Fafarman, *Nano Lett.*, 2016, **16**, 3563–3570.
26 E. T. Hoke, D. J. Slotcavage, E. R. Dohner, A. R. Bowring, H. I. Karunadasa and M. D. McGehee, *Chem. Sci.*, 2015, **6**, 613–617.
27 B.-w. Park, B. Philippe, S. M. Jain, X. Zhang, T. Edvinsson, H. Rensmo, B. Zietz and G. Boschloo, *J. Mater. Chem. A*, 2015, **3**, 21760–21771.
28 C. M. Sutter-Fella, Y. Li, M. Amani, J. W. Ager, 3rd, F. M. Toma, E. Yablonovitch, I. D. Sharp and A. Javey, *Nano Lett.*, 2016, **16**, 800–806.
29 A. Y. Chang, Y.-J. Cho, K.-C. Chen, C.-W. Chen, A. Kinaci, B. T. Diroll, M. J. Wagner, M. K. Y. Chan, H.-W. Lin and R. D. Schaller, *Adv. Energy Mater.*, 2016, **6**, 1600422.
30 H. Wang, L. Valkunas, T. Cao, L. Whittaker-Brooks and G. R. Fleming, *J. Phys. Chem. Lett.*, 2016, **7**, 3284–3289.
31 L. Wang, C. McCleese, A. Kovalsky, Y. Zhao and C. Burda, *J. Am. Chem. Soc.*, 2014, **136**, 12205–12208.
32 S. J. Yoon, S. Draguta, J. S. Manser, O. Sharia, W. F. Schneider, M. Kuno and P. V. Kamat, *ACS Energy Lett.*, 2016, **1**, 290–296.
33 W. Rehman, D. P. McMeekin, J. B. Patel, R. L. Milot, M. B. Johnston, H. J. Snaith and L. M. Herz, *Energy Environ. Sci.*, 2017, **10**, 361–369.
34 W. Rehman, R. L. Milot, G. E. Eperon, C. Wehrenfennig, J. L. Boland, H. J. Snaith, M. B. Johnston and L. M. Herz, *Adv. Mater.*, 2015, **27**, 7938–7944.
35 S. J. Yoon, K. G. Stamplecoskie and P. V. Kamat, *J. Phys. Chem. Lett.*, 2016, **7**, 1368–1373.
36 N. Marinova, S. Valero and J. L. Delgado, *J. Colloid Interface Sci.*, 2017, **488**, 373–389.
37 Y. Shi, Y. Xing, Y. Li, Q. Dong, K. Wang, Y. Du, X. Bai, S. Wang, Z. Chen and T. Ma, *J. Phys. Chem. C*, 2015, **119**, 15868–15873.
38 Z. Guo, Y. Wan, M. Yang, J. Snaider, K. Zhu and L. Huang, *Science*, 2017, **356**, 59–62.
39 E. Edri, S. Kirmayer, M. Kulbak, G. Hodes and D. Cahen, *J. Phys. Chem. Lett.*, 2014, **5**, 429–433.
40 L. Etgar, P. Gao, Z. Xue, Q. Peng, A. K. Chandiran, B. Liu, M. K. Nazeeruddin and M. Gratzel, *J. Am. Chem. Soc.*, 2012, **134**, 17396–17399.
41 J. Burschka, N. Pellet, S.-J. Moon, R. Humphry-Baker, P. Gao, M. K. Nazeeruddin and M. Grätzel, *Nature*, 2013, **499**, 316–319.
42 J. H. Noh, S. H. Im, J. H. Heo, T. N. Mandal and S. I. Seok, *Nano Lett.*, 2013, **13**, 1764–1769.
43 L. Gil-Escrig, A. Miquel-Sempere, M. Sessolo and H. J. Bolink, *J. Phys. Chem. Lett.*, 2015, **6**, 3743–3748.
44 N.-G. Park, *J. Phys. Chem. Lett.*, 2013, **4**, 2423–2429.
45 S. D. Stranks and H. J. Snaith, *Nat. Nanotechnol.*, 2015, **10**, 391–402.
46 R. G. Niemann, A. G. Kontos, D. Palles, E. I. Kamitsos, A. Kaltzoglou, F. Brivio, P. Falaras and P. J. Cameron, *J. Phys. Chem. C*, 2016, **120**, 2509–2519.

 This journal is © The Royal Society of Chemistry 2017

Published on 02 August 2017. Downloaded by University of Tennessee at Knoxville on 14/08/2017 21:56:08.

47 V. A. Hintermayr, A. F. Richter, F. Ehrat, M. Doblinger, W. Vanderlinden, J. A. Sichert, Y. Tong, L. Polavarapu, J. Feldmann and A. S. Urban, *Adv. Mater.*, 2016, **28**, 9478–9485.
48 Y. Tong, E. Bladt, M. F. Ayguler, A. Manzi, K. Z. Milowska, V. A. Hintermayr, P. Docampo, S. Bals, A. S. Urban, L. Polavarapu and J. Feldmann, *Angew. Chem., Int. Ed.*, 2016, **55**, 13887–13892.
49 P. Piatkowski, B. Cohen, F. J. Ramos, M. Di Nunzio, M. K. Nazeeruddin, M. Gratzel, S. Ahmad and A. Douhal, *Phys. Chem. Chem. Phys.*, 2015, **17**, 14674–14684.
50 T. C. Sum, N. Mathews, G. Xing, S. S. Lim, W. K. Chong, D. Giovanni and H. A. Dewi, *Acc. Chem. Res.*, 2016, **49**, 294–302.
51 G. Xing, N. Mathews, S. Sun, S. S. Lim, Y. M. Lam, M. Grätzel, S. Mhaisalkar and T. C. Sum, *Science*, 2013, **342**, 344–347.
52 S. S. Lim, W. K. Chong, A. Solanki, H. A. Dewi, S. Mhaisalkar, N. Mathews and T. C. Sum, *Phys. Chem. Chem. Phys.*, 2016, **18**, 27119–27123.
53 J. S. Manser, J. A. Christians and P. V. Kamat, *Chem. Rev.*, 2016, **116**, 12956–13008.
54 J. S. Manser and P. V. Kamat, *Nat. Photonics*, 2014, **8**, 737–743.
55 G. R. Berdiyorov, F. El-Mellouhi, M. E. Madjet, F. H. Alharbi, F. M. Peeters and S. Kais, *Sol. Energy Mater. Sol. Cells*, 2016, **148**, 2–10.
56 E. M. L. D. de Jong, G. Yamashita, L. Gomez, M. Ashida, Y. Fujiwara and T. Gregorkiewicz, *J. Phys. Chem. C*, 2017, **121**, 1941–1947.
57 M. Li, S. Bhaumik, T. W. Goh, M. S. Kumar, N. Yantara, M. Gratzel, S. Mhaisalkar, N. Mathews and T. C. Sum, *Nat. Commun.*, 2017, **8**, 14350.
58 M. B. Price, J. Butkus, T. C. Jellicoe, A. Sadhanala, A. Briane, J. E. Halpert, K. Broch, J. M. Hodgkiss, R. H. Friend and F. Deschler, *Nat. Commun.*, 2015, **6**, 9420.
59 J. Yang, X. Wen, H. Xia, R. Sheng, Q. Ma, J. Kim, P. Tapping, T. Harada, T. W. Kee, F. Huang, Y. B. Cheng, M. Green, A. Ho-Baillie, S. Huang, S. Shrestha, R. Patterson and G. Conibeer, *Nat. Commun.*, 2017, **8**, 14120.
60 A. P. Kirk and M. V. Fischetti, *Phys. Rev. B: Condens. Matter*, 2012, **86**, 165206.
61 C. C. Stoumpos, C. D. Malliakas and M. G. Kanatzidis, *Inorg. Chem.*, 2013, **52**, 9019–9038.
62 J. Su, D. P. Chen and C. T. Lin, *J. Cryst. Growth*, 2015, **422**, 75–79.
63 A. D. Wright, C. Verdi, R. L. Milot, G. E. Eperon, M. A. Perez-Osorio, H. J. Snaith, F. Giustino, M. B. Johnston and L. M. Herz, *Nat. Commun.*, 2016, **7**, 11755.
64 E. M. Talbert, H. F. Zarick, N. J. Orfield, W. Li, W. R. Erwin, Z. R. DeBra, K. R. Reid, C. P. McDonald, J. R. McBride, J. Valentine, S. J. Rosenthal and R. Bardhan, *RSC Adv.*, 2016, **6**, 86947–86954.
65 M. E.-A. Madjet, A. V. Akimov, F. El-Mellouhi, G. R. Berdiyorov, S. Ashhab, N. Tabeta and S. Kaisac, *Phys. Chem. Chem. Phys.*, 2016, **18**, 5219–5231.
66 D. J. Slotcavage, H. I. Karunadasa and M. D. McGehee, *ACS Energy Lett.*, 2016, **1**, 1199–1205.
67 X. Deng, X. Wen, S. Huang, R. Sheng, T. Harada, T. W. Kee, M. Green and A. Ho-Baillie, *J. Phys. Chem. C*, 2016, **120**, 2542–2547.
68 T. C. Sum and N. Mathews, *Energy Environ. Sci.*, 2014, **7**, 2518–2534.
69 Y. Yang, M. Yang, Z. Li, R. Crisp, K. Zhu and M. C. Beard, *J. Phys. Chem. Lett.*, 2015, **6**, 4688–4692.
70 Z. Zhu, J. Ma, Z. Wang, C. Mu, Z. Fan, L. Du, Y. Bai, L. Fan, H. Yan, D. L. Phillips and S. Yang, *J. Am. Chem. Soc.*, 2014, **136**, 3760–3763.
71 L. H. Manger, M. B. Rowley, Y. Fu, A. K. Foote, M. T. Rea, S. L. Wood, S. Jin, J. C. Wright and R. H. Goldsmith, *J. Phys. Chem. C*, 2017, **121**, 1062–1071.
72 W. R. Erwin, H. F. Zarick, E. M. Talbert and R. Bardhan, *Energy Environ. Sci.*, 2016, **9**, 1577–1601.
73 H. F. Zarick, A. Boulesbaa, A. A. Puretzky, E. M. Talbert, Z. R. DeBra, N. Soetan, D. B. Geohegan and R. Bardhan, *Nanoscale*, 2017, **9**, 1475–1483.